14th World Congress in Computational Mechanics (WCCM)
ECCOMAS Congress 2020
Virtual Congress: 11 – 15 January 2021
F. Chinesta, R. Abgrall, O. Allix and M. Kaliske (Eds)

NUMERICAL SIMULATION OF FLOW IN A FUEL-INJECTOR OF AN AIRCRAFT ENGINE COMBUSTOR USING BUILDING-CUBE METHOD

Younghwa Cho[1], Rahul Bale[2], Makoto Tsubokura[3], and Nobuyuki Oshima[4]

[1] School of Engineering, Hokkaido University
Kita 13, Nishi 8, Kita-ku, Sapporo, Hokkaido 060-8628, Japan
E-mail: younghwa@eis.hokudai.ac.jp, URL: https://www.eng.hokudai.ac.jp/english/

[2] RIKEN Center for Computational Science (R-CCS)
7-1-26 Minatojima-minami-machi, Chuo-ku, Kobe, Hyogo 650-0047, Japan
E-mail: rahul.bale@riken.jp, URL: https://www.r-ccs.riken.jp/en/

[3] RIKEN Center for Computational Science (R-CCS)
7-1-26 Minatojima-minami-machi, Chuo-ku, Kobe, Hyogo 650-0047, Japan
E-mail: mtsubo@riken.jp, URL: https://www.r-ccs.riken.jp/en/

[4] School of Engineering, Hokkaido University
Kita 13, Nishi 8, Kita-ku, Sapporo, Hokkaido 060-8628, Japan
E-mail: oshima@eng.hokudai.ac.jp, URL: https://www.eng.hokudai.ac.jp/english/

Keywords: Building-Cube Method, Immersed Boundary Method, Grid-Dependency, Aircraft Engine Combustor.

Abstract. In this study, we investigate grid dependency on local mesh refinement for the numerical simulation of cold flow in an aircraft engine's fuel-injector. The numerical simulation of fully compressible Navier-Stokes equations is conducted using a hierarchical Cartesian mesh-based solver known as "CUBE". Using the results of the high-resolution simulation as the basis, the gird dependency analysis is carried out. In addition, we evaluate the weak scaling of the underlying solver.

1 INTRODUCTION

The geometry of an aircraft engine's industrial-scale fuel-injector is considerably sophisticated, and computer-aided design (CAD) data are usually burdened with geometric imperfections: 'dirtiness.' This makes a mesh generation be an extremely time-consuming task. Furthermore, the computational load of the numerical mesh generation becomes enormous to resolve geometric complexities and boundary layers appropriately. required to resolve geometric complexities and boundary layers is enormous. Therefore, it is necessary to develop strategies for easing mesh generation and computational load. Accordingly, to ease the mesh generation and immersed boundary method (IBM) for handling complex non-watertight

geometries, we adopt a hierarchical Cartesian meshing technique known as the building-cube method (BCM). Focusing on the cold flow simulation of a fuel-injector of an aircraft engine, this study presents an investigation on grid dependency; here, the cold flow simulations are conducted by a fully compressible flow solver of a BCM-based numerical framework named "CUBE". In addition, the scalability performance of CUBE is evaluated by a massively parallel computer system "FUGAKU" and it exhibits optimal scalability.

2 NUMERICAL FRAMEWORK

2.1 Building-Cube Method

The numerical framework adopted in this study is based on a solver known as CUBE, which is built on a Cartesian meshing methodology known as BCM [1, 2]. In BCM, the computational domain is discretized into cubic blocks referred to as cubes. In addition, finer cubes can be populated in the region of interest, such as the target geometry. In this study, the refinement ratio of the size of adjacent cubes with different sizes is restricted to two. Each cube in the domain is subdivided into cubic cells such that all cubes have the same number of cells. Because a cube is handled as the fundamental unit of the mesh data structure, the computational cost of every cube is identical, thus making the domain decomposition straightforward. A schematic representation of the discretization procedure using BCM is presented in **Figure 1**.

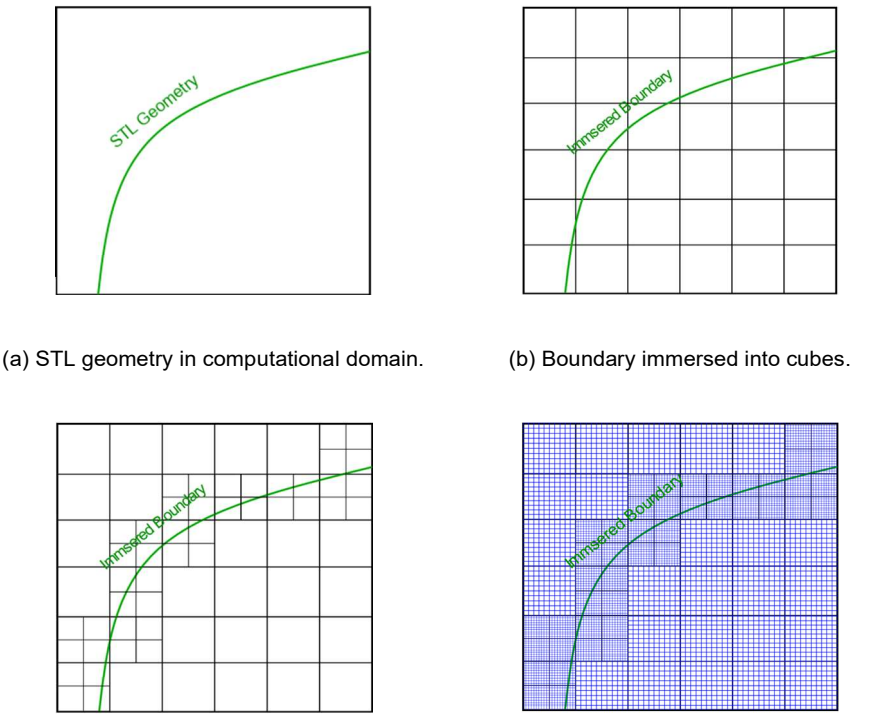

(a) STL geometry in computational domain.

(b) Boundary immersed into cubes.

(c) Subdivision of cubes in the domain.

(d) Cell (blue) generation in each cube.

Figure 1: Schematic of discretization procedure using BCM

2.2 Immersed Boundary Method

The geometry of an aircraft engine's fuel-injector is considerably sophisticated, and the industrial-scale CAD data are usually non-watertight. Many IB methods that can be found in the literature are generally not well-suited for treating non-watertight CAD data. For such IBMs, additional time is required for preprocessing the data. However, the IBM developed by Li, *et al.* [3] addresses this limitation and allows CAD geometry to be non-watertight, thereby eliminating the effort required for preprocessing. In this work we empoy the IBM of Li, *et al.*.

2.3 Governing Equations

In this study, we adopt fully compressible Navier-Stokes equations, and the compact form is expressed as:

$$\frac{\partial \boldsymbol{Q}}{\partial t} + \boldsymbol{\nabla} \cdot \boldsymbol{F} = \boldsymbol{0}, \tag{1}$$

where

$$\boldsymbol{Q} = \begin{pmatrix} \rho \\ \rho u_1 \\ \rho u_2 \\ \rho u_3 \\ \rho e \end{pmatrix}, \boldsymbol{F}_i = \begin{pmatrix} \rho u_i \\ \rho u_i u_1 + p\delta_{i1} - \tau_{i1} \\ \rho u_i u_2 + p\delta_{i2} - \tau_{i2} \\ \rho u_i u_3 + p\delta_{i3} - \tau_{i3} \\ (\rho e + p)u_i - \tau_{ij}u_j + q_i \end{pmatrix}.$$

Here, $\rho, \boldsymbol{u}, e, p, \boldsymbol{q}$ and $\boldsymbol{\tau}$ represent the density of the gas phase, velocity, total energy per unit of mass, pressure, heat flux vector, and shear stress tensor, respectively. The total energy per unit mass is defined as:

$$e = \frac{p}{\rho(\gamma - 1)} + \frac{1}{2} u_i u_i, \tag{3}$$

where γ is the specific heat ratio. The heat flux $\boldsymbol{q}$ is given by:

$$\boldsymbol{q} = -\lambda \boldsymbol{\nabla} T, \tag{4}$$

where λ and T represent the thermal conductivity and temperature, respectively. In addition, the shear stress tensor $\boldsymbol{\tau}$ is given as:

$$\tau_{ij} = \mu \left(2S_{ij} - \frac{2}{3} \delta_{ij} \frac{\partial u_k}{\partial x_k} \right), \tag{5}$$

where $\boldsymbol{S}$ is the strain-rate tensor expressed as:

$$S_{ij} = \frac{1}{2} \left(\frac{\partial u_j}{\partial x_i} + \frac{\partial u_i}{\partial x_j} \right). \tag{6}$$

Finally, the discretization methodologies are presented in **Table 1**. The simulation adopted in this study is a large-eddy simulation with an implicit sub-grid scale (SGS) model. Here, the numerical dissipation added through the Roe-upwinding scheme is assumed to function as a

proxy for the SGS model, while the grid size serves as the spatial filter.

Table 1: Discretization methodologies adopted in this study

Time Marching	Low-Mach Preconditioned Lower-Upper Symmetric Gauss-Seidel (LU-SGS) with Solution Limited Time-Stepping (SLTS) [4, 5, 6]
Advective Flux Term	Low-Mach Preconditioned Roe with 5th-Order MUSCL [4, 7, 8]
Diffusive Flux Term	2nd-Order Central Difference

3 INVESTIGATION OF GRID DEPENDENCY

3.1 Geometry of Reference Fuel-Injector

The reference fuel-injector, an ECO-SGS type fuel-injector, was provided by Kawasaki Heavy Industries, Ltd. (KHI), and the CAD data (STL format) are presented in **Figure 3-(a)**. In addition, the diameter D of the fuel-injector, axial length L, and width of the air-slit nozzle W are approximately 62 [mm], 60 [mm], and 1 [mm], respectively.

There are three types of paths in the pilot nozzle as illustrated in **Figure 3-(b)**. Furthermore, the inflow-plane is arranged to introduce inflow boundary conditions, and the reference fuel-injector is combined with a duct to guide the influx of flow from the inflow-plane. The arrangement of the geometries, as well as an example of the BCM mesh around the geometries, is presented in **Figure 3-(c)**.

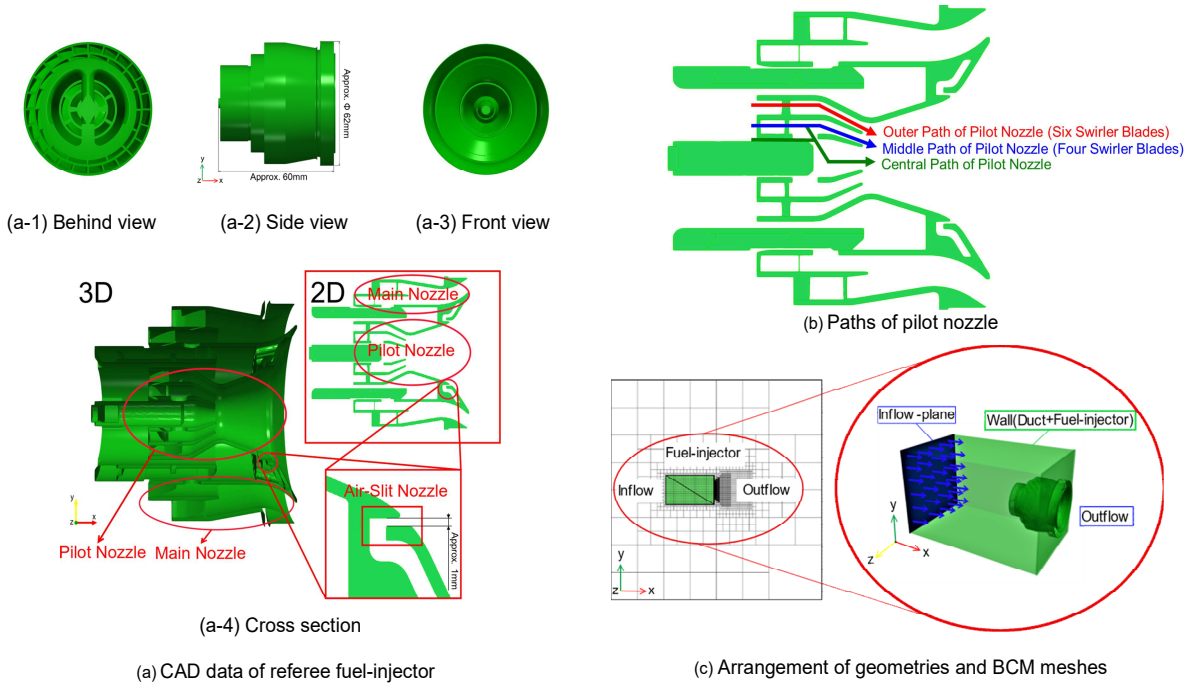

Figure 3: CAD data of referee fuel-injector and the arrangement of the geometries in the computational domain

3.2 Reference Experimental Condition and Computational Setup

In this study, an operational condition of the experiment conducted by Kawasaki Heavy Industries, Ltd. (KHI) is referenced to establish the computational setup of this study. The experimental condition is presented in **Table 2**.

Table 2: Reference experimental condition, provided by KHI

Ambient Pressure	1 [atm]
Ambient Temperature	288.15 [K]
Inflow Mass Flow Rate	0.074 [kg/s]
Inner Pressure of Duct	1.05 [atm]

In the computational domain, no-slip, and adiabatic conditions are applied to the wall. The velocity applied in the inflow-plane is estimated such that the inflow mass flow rate becomes the same value presented in **Table 2**, whereas the velocity applied on the inflow-plane is $\mathbf{u} = (5.376, 0, 0)$ [m/s]. In addition, the initial condition is tabulated in **Table 3**. Density is calculated using the equation of state for ideal gas from the ambient temperature and pressure presented in **Table 2**.

Table 3: Initial condition applied to the entire domain this study

Density	1.225 [kg/m^3]
Pressure	1 [atm]
Velocity	$(u, v, w) = (5.376, 0.000, 0.000)$ [m/s]

3.3 Meshes

For the investigation on grid dependency, we consider three meshes: (1) Mesh1- smallest mesh spacing of 0.095 [mm] and mesh size of 25 M, (2) Mesh2- smallest mesh spacing of 0.076 [mm] and mesh size of 120 M, and (3) Mesh3- smallest mesh spacing of 0.050 [mm] and mesh size of 500 M (See **Figure 4**). Although there is a significant deviation in mesh size, the difference in the time consumed for the mesh generation is negligible, and it is approximately within 0.5 [h].

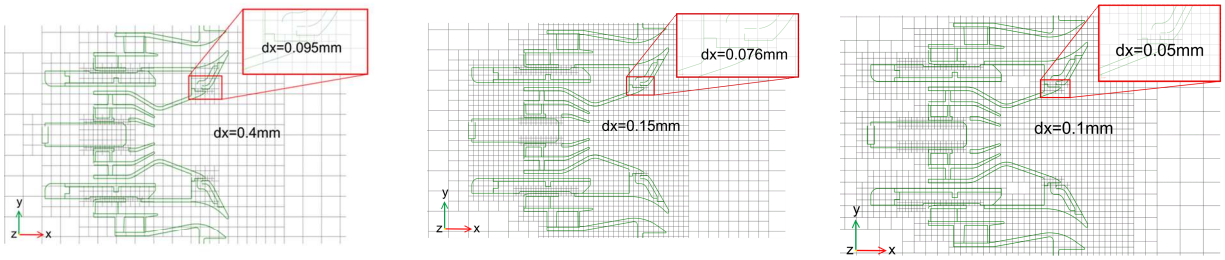

(a) Mesh1 (Size: 25,000,000) (b) Mesh2 (Size: 120,000,000) (c) Mesh3 (Size: 500,000,000)

Figure 4: Meshes used for the grid dependency investigation

3.4 Results

3.4.1 Results of Inner Pressure of Duct

First, the inner pressure transition of the duct is illustrated in **Figure 5**. In the range of 0–1000-time steps (: shaded part), the profile exhibits initial transiency. Therefore, in this simulation, the average in time is considered in the range of 2000–4000-time steps, where the profile is stationary, and the averaged inner pressure of the duct is presented in **Figure 6**. As presented in **Figure 6**, the inner pressure of duct becomes smaller as the grid becomes finer, and it converges to the referenced condition presented in **Table 2**. For Mesh3, the averaged pressure exhibit reasonable value within 1% of the reference value. However, because the difference between Mesh2 and Mesh3 is still noticeable, we need to examine more refined case for checking the convergence.

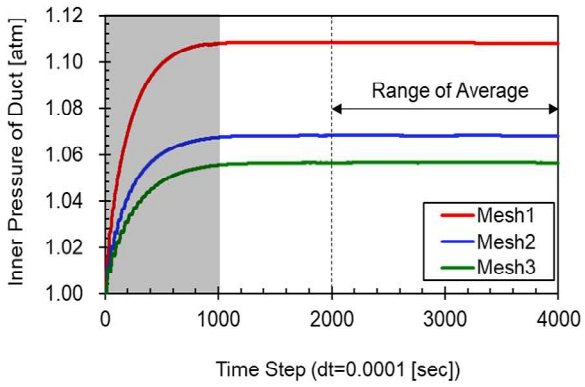

Figure 5: Inner pressure profile of duct

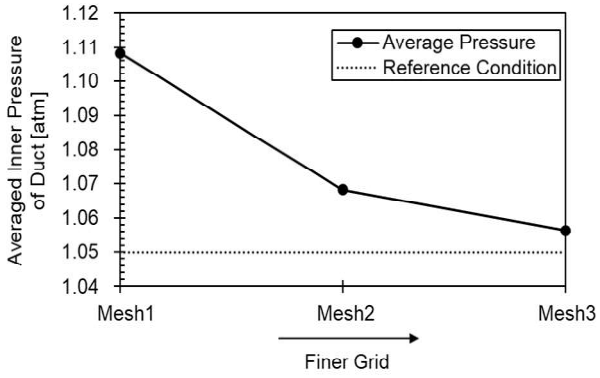

Figure 6: Inner pressure change depending on grid

3.4.2 Results of Averaged Velocity and Pressure Distribution

3.4.2.1 Comparison of Mesh1 and Mesh3

As illustrated in **Figure 4**, in Mesh1, the finest resolution of $dx = 0.095\ [mm]$ is assigned in the narrowest parts represented by the air-slit nozzle, thereby making Mesh1 approximately two times coarser than Mesh3.

The results of the simulation, where Mesh1 was adopted, is presented in **Figure 7-(a)**. This indicates that although Mesh1 was two times coarser than Mesh3, it was able to resolve the flow through the air-slit nozzle. However, in the region of flow from pilot nozzle (A-region), a significant difference between Mesh1 and Mesh3 is depicted in **Figure 7-(c)**. In the Mesh3 case, the flow from the pilot nozzle (A-region) is attached to the wall. However, in the Mesh1 case, its counterpart is developed as jet flow, separating it from the wall. Therefore, the A-region near the exit of the pilot nozzle appears to be a susceptible region that significantly influences the flow. In contrast, A-region of Mesh3 exhibits negative pressure. The negative pressure region is considered to be established by the flow attached to the wall, and because the flow is not attached to the wall in Mesh1, the A-region does not exhibit negative pressure.

Another difference in flow between Mesh1 and Mesh3 indicates the difference in the

distribution of velocity magnitude in the B- and C-regions. The velocity magnitude in B-region of Mesh1 is larger than its Mesh3 counterpart. Contrastively, the velocity magnitude in C-region of Mesh1 is smaller than its Mesh3 counterpart. Owing to the small magnitude of velocity, it can be stated that the swirl from the pilot nozzle is incompletely developed in the Mesh1 case. In addition, the pressure distribution in the B- and C-regions indicates that the pressure gradient of Mesh3 becomes more moderate than its Mesh1 counterpart. This suggests that the resolution of Mesh1 in the region is insufficient such that more pressure gradients were required to pass through the region, especially the outer path of pilot nozzle (**Figures 3-(b)** and **7-(a)**). Therefore, it can be stated that because most of the flow of the pilot nozzle passed through the central path, where the swirl effect does not appear, the swirl in the A-region became weak; hence, no negative pressure appeared in the A-region, and jet flow was developed.

In summary, Mesh1 was successfully able to resolve all flow-paths in the geometry. However, the result is remarkable because the flow and pressure distribution in the A-region (pilot region) do not qualitatively agree with its counterpart in Mesh3. Consequently, it is inferred that the pilot region exhibits the highest dependency upon resolution change.

3.4.2.2 Comparison of Mesh2 and Mesh3

As illustrated in **Figure 5**, in Mesh2, the resolution of the air-slit nozzle is selected to be $dx = 0.076\ [mm]$. As is evident from the analysis of the results obtained from Mesh1, the pilot region is highly sensitive to resolution. Therefore, for the present mesh, *i.e.*, Mesh2, a mesh spacing of 0.15 [mm] is selected for the pilot region, which is 0.4 [mm] in Mesh1.

The simulation results, where Mesh2 was adopted, is presented in **Figure 7-(b)**. It is evident from the result that Mesh2 was successfully able to capture the flow attached to the wall of the pilot nozzle. The velocity and pressure distribution of air-slit nozzle exhibit good agreement with its Mesh3 counterparts. In addition, the distribution of velocity magnitudes in the B- and C-regions is also considerably consistent with its counterpart in Mesh3. However, focusing on the pressure distribution, the pressure gradient in Mesh3 is more moderate than its counterpart in Mesh2, and the A-region of Mesh3 exhibits a stronger negative pressure than its Mesh2 counterpart. Considering that the pressure gradient along the flow demonstrates the flow path's resistance, the following can be stated: because, in Mesh3, the outer path of the pilot nozzle (**Figure 3-(b)**) exhibits more moderate pressure gradient than that of Mesh2 (**Figures 7-(b-2, c-2)**), more flow passes through the outer path, and a stronger swirl is can be formed in the pilot nozzle. It is considered that this stronger swirl contributes to the stronger negative pressure in the A-region of Mesh3. In addition, another difference between Mesh2 and Mesh3 can be found in **Figure 8**. In the Mesh2 case (**Figure 8-(a)**), the swirl flow from the middle path of the pilot nozzle, which has four swirler blades, appears significantly in the plane of $x = 0$ [m], although it does not appear on the outer path of the pilot nozzle, which has 6 swirler blades. However, in the Mesh3 case (**Figure 8-(b)**), because the swirl from the outer path becomes more significant, and that from the middle path becomes dissipated by joining the outer swirl, the swirl from the outer path significantly appears in the plane of $x = 0$ [m]. This indicates that Mesh2 was unable to accurately reproduce the 3D structure of the swirl in pilot region (A- and C-regions). Accordingly, it can be inferred that the pilot region still exhibits grid dependency between Mesh2 and Mesh3.

Based on the results obtained from Mesh1, Mesh1 was able to identify the key regions that significantly influence the flow, and generate a new mesh accordingly- Mesh2. Therefore, regarding the A-, B-, and C-regions illustrated in **Figure 7**, Mesh2 obtained results consistent with those of Mesh3. However, as shown in **Figure 8**, Mesh2 was actually unable to accurately reproduce the 3D structure of the swirl in the pilot region. Therefore, in future works, it is necessary to conduct this study using finer grid instead of Mesh3.

4 WEAK SCALING EVALUATION

In this evaluation, we solely consider the fully compressible Navier-Stokes solver. The evaluation was conducted using meshes whose size are 1179648, 9437184, 75497472, 603979776 and 3505070080, whereas the simulations were carried out using 192, 1536, 12288, 98304 and 576000 CPUs, respectively. Here, the speedup ratio is defined as:

$$\text{Speedup Ratio} = \frac{\text{Runtime-Per-Timestep of Basis Mesh} \times \frac{\text{Target Mesh Size}}{\text{Basis Mesh Size}}}{\text{Runtime-Per-Timestep of Target Mesh}}. \tag{7}$$

In this study, the basis mesh is set as the smallest mesh with a size of 1179648. The weak scaling results are plotted in **Figure 9**, and the simulation exhibits excellent scalability in the range of the set of mesh-CPUs considered in this study. In addition, the parallel efficiency at 576000 CPUs (mesh size: 3505070080) is 75.5%.

5 CONCLUSIONS

Using the imperfect CAD data of an aircraft engine's fuel-injector, a study on grid dependency, as well as weak scaling evaluation, was conducted. The conclusions drawn from the study are summarized as follows.

Firstly, in the investigation on the inner pressure of the duct, the grids chosen in this study for the cold flow simulation of the fuel-injector showed positive convergence towards the reference experimental duct pressure. While the agreement between the pressure of mesh3 and reference value is acceptable, it may be possible to improve the results marginally using a more refined mesh.

Also, between Mesh2 and Mesh3, the velocity and pressure distribution agreed well in **Figure 7**. However, as shown in **Figure 8**, the 3D structure of the pilot region's swirl differed between Mesh2 and Mesh3. Thus, it can be said that the most sensitive region was the pilot region (A- and C-regions). In particular, the paths that include the swirler (*i.e.*, the outer and middle paths illustrated in **Figure 3-(b)**) function as key regions of the grid dependency. As a future work, it is necessary to investigate more refined (larger) cases than Mesh3 to study the mesh dependency.

Finally, through the weak scaling evaluation, it has been demonstrated that the present simulation with CUBE exhibits optimal parallel efficiency with approximately seven times larger cases than Mesh3, which is the largest mesh size used in the present study on grid dependency. Therefore, even in more refined cases, the effective parallel computation can also be expected.

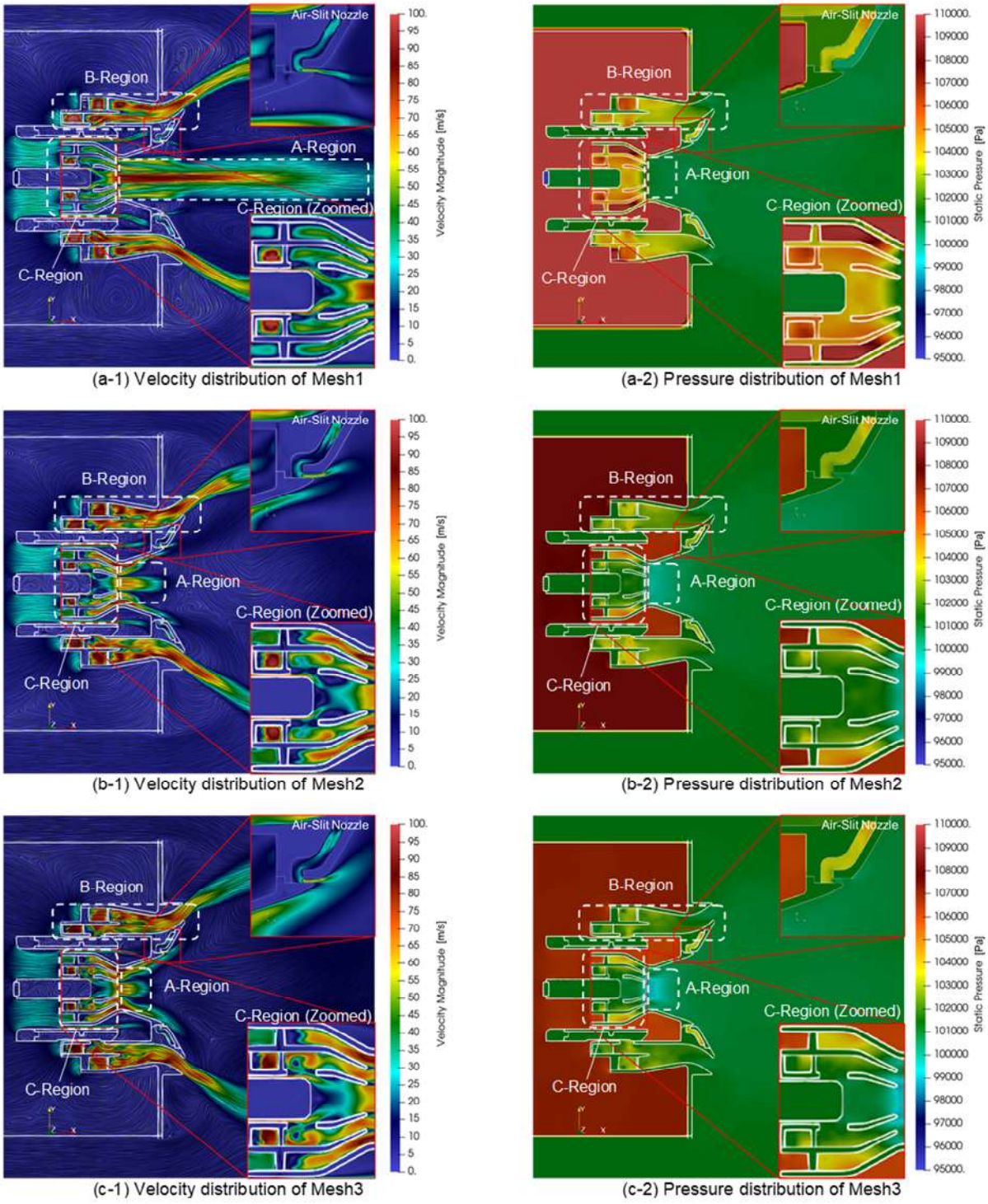

Figure 7: Averaged velocity and pressure distribution of each mesh

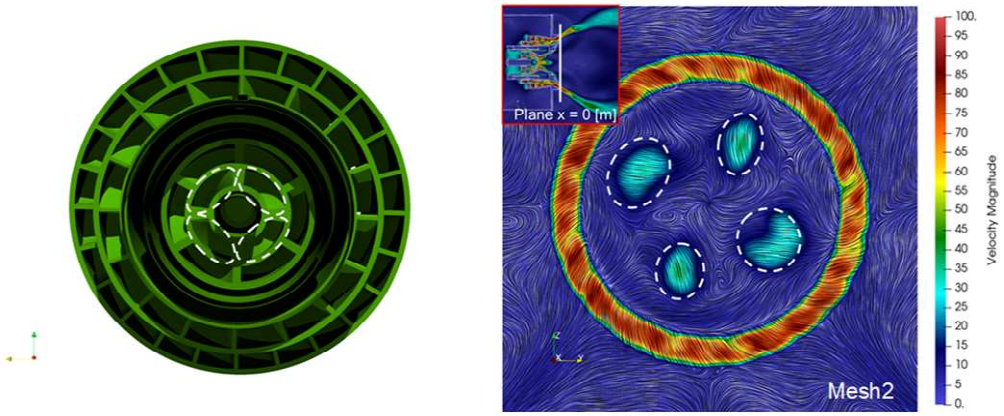

(a) Number of blades in middle path of pilot nozzle (left) and velocity distribution of mesh2 at plane x = 0 [m] (right)

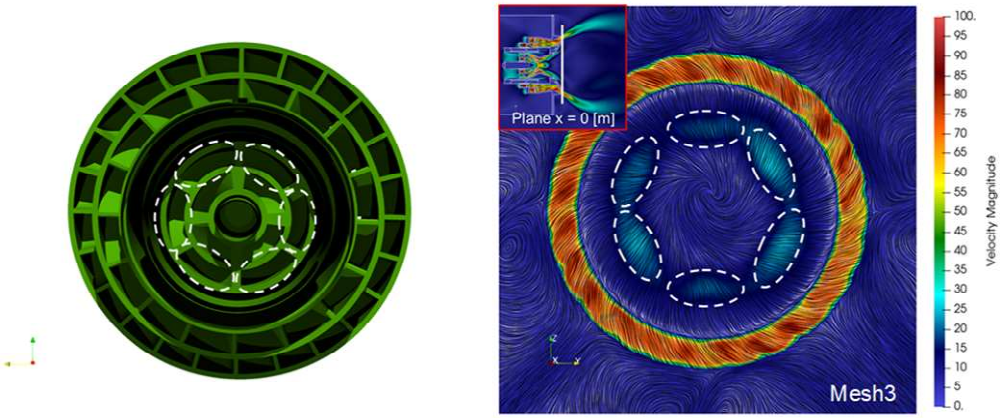

(b) Number of blades in outer path of pilot nozzle (left) and velocity distribution of mesh3 at plane x = 0 [m] (right)

Figure 8: Averaged velocity distribution at plane x = 0 [m] of Mesh2 and Mesh3

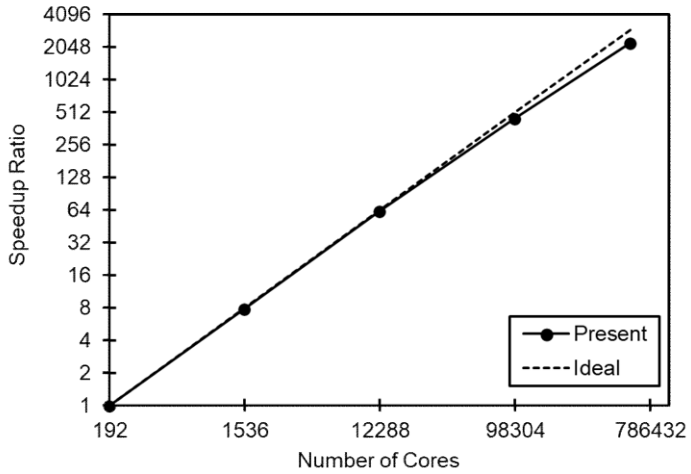

Figure 9: Speedup ratio against the number of CPUs of a fully compressible flow simulation

ACKNOWLEDGEMENT

This work was carried out under a collaboration between Hokkaido University, RIKEN, Center for Computational Science, and Kawasaki Heavy Industries, Ltd.. This work employed computational resources of the supercomputer, "FUGAKU", provided by RIKEN via the HPCI System Research Project (Project ID: hp200160) and supercomputer "ITO" provided by the Research Institute for Information Technology, Kyushu University (Project ID: hp200017), as well as the supercomputer "Grand Chariot" provided by the Information Initiative Center, Hokkaido University, Japan. This work was also supported by f^3 Engineering Education and Research Center, Faculty of Engineering, Hokkaido University, Japan. Finally, Kenta Takami, an undergraduate student at Hokkaido University, is acknowledged for research assistance.

REFERENCES

[1] JANSSON, Niclas, *et al.* CUBE: A scalable framework for large-scale industrial simulations. The international journal of high performance computing applications, 2019, 33.4: 678–698.

[2] NAKAHASHI, Kazuhiro. Building-cube method for flow problems with broadband characteristic length. In: Computational fluid dynamics 2002. Springer, Berlin, Heidelberg, 2003, 77–81.

[3] LI, Chung-Gang; TSUBOKURA, Makoto; BALE, Rahul. Framework for simulation of natural convection in practical applications. International Communications in Heat and Mass Transfer, 2016, 75: 52–58.

[4] WEISS, Jonathan M.; SMITH, Wayne A. Preconditioning applied to variable and constant density flows. AIAA journal, 1995, 33.11: 2050–2057.

[5] YOON, Seokkwan; JAMESON, Antony. Lower-upper symmetric-Gauss-Seidel method for the Euler and Navier-Stokes equations. AIAA journal, 1988, 26.9: 1025–1026.

[6] LIAN, Chenzhou; XIA, Guoping; MERKLE, Charles L. Solution-limited time stepping to enhance reliability in CFD applications. Journal of Computational Physics, 2009, 228.13: 4836–4857.

[7] ROE, Philip L. Approximate Riemann solvers, parameter vectors, and difference schemes. Journal of computational Physics, 1997, 135.2: 250–258.

[8] KIM, Kyu Hong; KIM, Chongam. Accurate, efficient and monotonic numerical methods for multi-dimensional compressible flows: Part II: Multi-dimensional limiting process. Journal of computational physics, 2005, 208.2: 570–615.